

1 **Rheologic constraints on the upper mantle from five years of**
2 **postseismic deformation following the El Mayor-Cucapah**
3 **earthquake**

4 **T. T. Hines¹, E. A. Hetland¹**

5 ¹Department of Earth and Environmental Sciences, University of Michigan, Ann Arbor, Michigan, USA.

6 **Key Points:**

- 7 • Transient postseismic deformation can be observed following the El Mayor-Cucapah
8 earthquake at epicentral distances of up to 400 km
9 • Near-field postseismic deformation exhibits early transience that decays to a sustained
10 rate which is elevated above the preseismic trend
11 • A Zener or Burgers upper mantle can explain far-field deformation while near-field tran-
12 sience can be described with afterslip

13 **Abstract**

14 Five years of postseismic deformation following the Mw7.2 El Mayor-Cucapah earthquake re-
 15 veals transient deformation that decays back to its pre-earthquake trend after about three years
 16 at epicentral distances greater than ~ 200 km. At closer distances, the rapid transience decays
 17 to a sustained rate which exceeds its pre-earthquake trend. We attempt to determine the mech-
 18 anisms driving this deformation, where we consider afterslip at seismogenic depths and vis-
 19 coelastic relaxation in the lower crust and upper mantle as candidate mechanisms. We find that
 20 early, rapid, near-field deformation can be explained with afterslip on the fault that ruptured
 21 coseismically, while the later, sustained, near-field deformation can be explained with either
 22 continued afterslip in an effectively elastic lower crust, or lower crustal viscoelastic relaxation
 23 with a steady-state viscosity of $\sim 10^{19}$ Pa s. The trend in far-field deformation is best explained
 24 with a transient viscosity of $\sim 10^{18}$ Pa s in the upper mantle. We argue that a transient rhe-
 25 ology in the mantle is preferable over a Maxwell rheology because it better predicts the de-
 26 cay in postseismic deformation, and also because it does not conflict with the generally higher,
 27 steady-state viscosities inferred from studies of geophysical processes occurring over longer
 28 time-scales.

29 **1 Introduction**

30 Ground deformation in the years following a large (\gtrsim Mw7) earthquake provides insight
 31 into the mechanical behavior of the crust and upper mantle. It has long been recognized that
 32 interpretations of postseismic deformation can be ambiguous because multiple postseismic de-
 33 formation mechanisms can have qualitatively similar surface expressions [e.g. Savage, 1990].
 34 Owing to the dense geodetic network deployed throughout the 2000s as part of the Plate Bound-
 35 ary Observatory, the postseismic deformation following the April 4, 2010, Mw7.2 El Mayor-
 36 Cucapah earthquake in Baja California was observed at more GPS stations than any other earth-
 37 quake in California to date. With such a large collection of data, we attempt to discern the mech-
 38 anisms driving postseismic deformation following the El Mayor-Cucapah earthquake, where
 39 we consider both afterslip and viscoelastic relaxation in the lower crust and upper mantle as
 40 candidate mechanisms.

41 Previous studies which have modeled postseismic deformation following the El Mayor-
 42 Cucapah earthquake include Pollitz *et al.* [2012], Gonzalez-Ortega *et al.* [2014], Spinler *et al.*
 43 [2015], and Rollins *et al.* [2015]. Of these studies, Gonzalez-Ortega *et al.* [2014] and Rollins
 44 *et al.* [2015] have attempted to describe the postseismic deformation with afterslip in an elas-
 45 tic half-space. Gonzalez-Ortega *et al.* [2014] described five months of postseismic deforma-
 46 tion, observed by InSAR and GPS within ~ 50 km of the rupture, with afterslip and contrac-
 47 tion on the coseismically ruptured fault. Gonzalez-Ortega *et al.* [2014] noted that their preferred
 48 model underestimated the GPS displacements for stations $\gtrsim 25$ km from the rupture and sug-
 49 gested that it could be the result of unmodeled viscoelastic relaxation. Using only continuous
 50 GPS stations, which are mostly north of the rupture zone, Rollins *et al.* [2015] found that three
 51 years of postseismic deformation can be adequately explained by afterslip, albeit with an im-
 52 plausibly large amount of slip inferred on the least constrained, southern-most fault segment.
 53 Here, we suggest the afterslip inferred by Rollins *et al.* [2015] may have been acting as a proxy
 54 for distributed relaxation in the upper mantle.

55 Pollitz *et al.* [2012], Rollins *et al.* [2015] and Spinler *et al.* [2015] have explored viscoelas-
 56 tic relaxation in the lower crust and upper mantle as a potential postseismic deformation mech-
 57 anism. The rheology of the crust and mantle is largely unknown and so modeling postseis-
 58 mic deformation with viscoelastic relaxation requires one to assume a rheologic model and
 59 then find the best fitting rheologic parameters. The inference of these rheologic parameters is
 60 a computationally expensive non-linear inverse problem which is typically approached with
 61 a forward modeling grid search method. Consequently, a simplified structure for the Earth must
 62 be assumed in order to minimize the number of rheologic parameters that need to be estimated.
 63 For example, it is commonly assumed that the lower crust and upper mantle are homogeneous,

Maxwell viscoelastic layers, which may be too simplistic for postseismic studies [Riva and Govers, 2009; Hines and Hetland, 2013]. To further reduce the dimensions of the model space, it is also necessary to make simplifying assumptions about the nature of afterslip. For example, one can assume a frictional model for afterslip and parametrize afterslip in terms of the unknown rheologic properties of the fault [e.g. Johnson *et al.*, 2009; Johnson and Segall, 2004]. One can also assume that afterslip does not persist for more than a few months and then model the later postseismic deformation assuming it to be the result of only viscoelastic relaxation [e.g. Pollitz *et al.*, 2012; Spinler *et al.*, 2015]. However, postseismic afterslip in similar tectonic settings has been observed to persist for decades following earthquakes [Çakir *et al.*, 2012; Cetin *et al.*, 2014]. Indeed, the preferred viscoelastic model from Pollitz *et al.* [2012] significantly underestimates deformation in the Imperial Valley, which could be indicative of unmodeled continued afterslip. Neglecting to allow for sustained afterslip as a postseismic mechanism could then lead to biased inferences of viscosities.

In this study, we perform a kinematic inversion for fault slip, allowing it to persist throughout the postseismic period, while simultaneously estimating the viscosity of the lower crust and upper mantle. We create an initial model of the fault slip and effective viscosity necessary to describe early postseismic deformation using the method described in Hines and Hetland [2016]. This method utilizes a first-order approximation of surface deformation resulting from viscoelastic relaxation which is only applicable to the early postseismic period. In this case, our initial model describes the first 0.8 years of postseismic deformation following the El Mayor-Cucapah earthquake. We then use the inferred effective viscosity structure from the initial model to create a suite of postseismic models to explain the five years of postseismic data available to date. Of the suite of models tested, we find that postseismic deformation following the El Mayor-Cucapah earthquake can be explained with a combination of afterslip on a fault segment running through the Sierra Cucapah and a Zener rheology in the upper mantle with a transient viscosity that decays from 6×10^{18} Pa s to 1×10^{18} Pa s at 120 km depth.

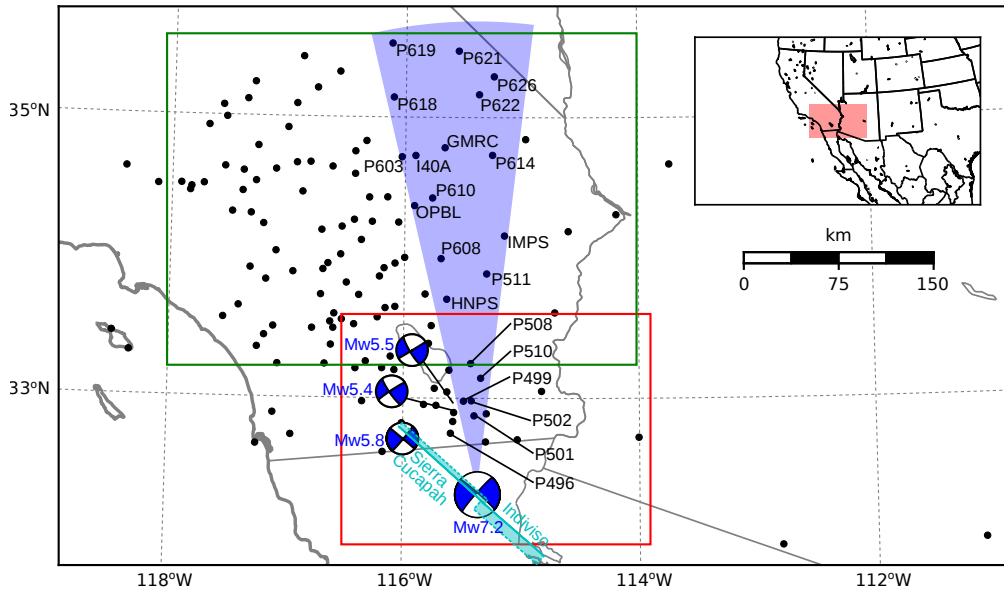
2 Data Processing

We use continuous GPS position time series provided by University Navstar Consortium (UNAVCO) for stations within a 400 km radius about the El Mayor-Cucapah epicenter. We collectively describe the coseismic and postseismic displacements resulting from the El Mayor-Cucapah earthquake as $u_{\text{post}}(t)$. We consider the GPS position time series $u_{\text{obs}}(t)$ to be the combination of $u_{\text{post}}(t)$, secular tectonic deformation, annual and semi-annual oscillations, and coseismic offsets from significant earthquakes over the time span of this study. The June 14, 2010, Mw5.8 Ocotillo earthquake and the Brawley swarm, which included an Mw5.5 and an Mw5.4 event on August 26, 2012, (Figure 1) are the only earthquakes that produced noticeable displacements in any of the time series. We treat the displacements resulting from the Brawley swarm as a single event because the daily solutions provided by UNAVCO cannot resolve the separate events. Although the Ocotillo earthquake had its own series of aftershocks [Hauksson *et al.*, 2011], neither the Ocotillo earthquake nor the Brawley swarm produced detectable postseismic deformation. We model displacements resulting from these events with only a Heaviside function, $H(t)$, describing the coseismic offsets. We then model $u_{\text{obs}}(t)$ as

$$u_{\text{obs}}(t) = u_{\text{pred}}(t) + \epsilon, \quad (1)$$

where

$$\begin{aligned} u_{\text{pred}}(t) = & u_{\text{post}}(t)H(t - t_{\text{emc}}) + c_0 + c_1 t + \\ & c_2 \sin(2\pi t) + c_3 \cos(2\pi t) + c_4 \sin(4\pi t) + c_5 \cos(4\pi t) + \\ & c_6 H(t - t_{\text{oc}}) + c_7 H(t - t_{\text{bs}}). \end{aligned} \quad (2)$$



91 **Figure 1.** Map of the region considered in this study. The large focal mechanism is for the El Mayor-
 92 Cucapah earthquake, and the three small focal mechanisms are for the Ocotillo earthquake and the two main
 93 shocks during the Brawley swarm. The black dots indicate the locations of GPS stations used in this study.
 94 The fault geometry used in this study is shown in cyan where dashed lines indicate buried edges of the fault
 95 segments. The green and red boxes demarcate the extent of the near-field and far-field maps (Figures 4 and 5).
 96 Stations inside the blue sector, which highlights the area within 10° of the El Mayor-Cucapah P axis, are used
 97 in Figures 7, 10, and 14

114 In the above equations, t_{emc} , t_{oc} and t_{bs} are the times of the El Mayor-Cucapah earthquake,
 115 Ocotillo earthquake, and the Brawley swarm, respectively, c_0 through c_7 are unknown coefficients,
 116 and ϵ is the observation noise. We only estimate jumps associated with the Ocotillo
 117 earthquake and Brawley swarm for stations within 40 km of their epicenters.

118 Stations which recorded displacements that clearly cannot be described by the aforementioned
 119 processes are not included in our analysis. This includes stations in the Los Angeles
 120 basin, where anthropogenic deformation can be larger than the postseismic signal that we are
 121 trying to estimate [Bawden *et al.*, 2001; Argus *et al.*, 2005]. In order to ensure an accurate es-
 122 timation of the secular deformation, we only use stations that were installed at least six months
 123 prior to El Mayor-Cucapah earthquake. Several GPS stations were installed after the El Mayor-
 124 Cucapah earthquake to improve the spatial resolution of postseismic deformation [Spinler *et al.*,
 125 2015]. Although it would be possible to subtract secular velocities derived from elastic block
 126 models [e.g. Meade and Hager, 2005] from velocities recorded at the newly installed stations
 127 to get an estimate of postseismic velocities, we do not do so here. We use coseismic and post-
 128 seismic displacements, rather than velocities, in our inverse method described in Section 3. We
 129 use displacements because estimating velocities from an already noisy displacement time se-
 130 ries can introduce significant uncertainties depending on exactly how the estimation is done.
 131 This choice prevents us from using the newly installed stations in Baja California for our anal-
 132 ysis.

133 The October 16, 1999, Mw7.1 Hector Mine earthquake, which occurred \sim 270 km north
 134 of the El Mayor-Cucapah epicenter, produced transient postseismic deformation which we do
 135 not wish to model, either mechanically or through empirical line fitting. We thus restrict our
 136 analysis to deformation observed six years after the Hector Mine earthquake, which is when
 137 postseismic velocities at sites proximal to the Hector Mine epicenter are approximately con-
 138 stant [Savage and Svare, 2009]. When appraising our model fit in Section 3, we see some sys-
 139 tematic residuals in the vicinity of the Hector Mine epicenter, which may be the result of er-
 140 rors in the assumption that the trend in Hector Mine postseismic deformation is linear after
 141 six years.

142 Studies of postseismic deformation typically assume a parametric form for $u_{\text{post}}(t)$, such
 143 as one with a logarithmic or exponential time dependence [e.g. Savage *et al.*, 2005]. However,
 144 by assuming a logarithmic or exponential form of $u_{\text{post}}(t)$ we run the risk of over fitting the
 145 GPS time series and inferring a non-existent postseismic signal. We therefore do not assume
 146 any parametric form for $u_{\text{post}}(t)$ and rather treat it as integrated Brownian motion, so that

$$\dot{u}_{\text{post}}(t) = \sigma^2 \int_0^t w(s) ds, \quad (3)$$

147 where $w(t)$ is white noise and the variance of $\dot{u}_{\text{post}}(t)$ increases linearly with time by a fac-
 148 tor of σ^2 . We use a Kalman filtering approach to estimate $u_{\text{post}}(t)$ and the unknown param-
 149 eters in eq. (2). In the context of Kalman filtering, our time varying state vector is

$$\mathbf{X}(t) = [u_{\text{post}}(t), \dot{u}_{\text{post}}(t), c_0, \dots, c_7] \quad (4)$$

150 and eq. (2) is the observation function which maps the state vector to the GPS observations.
 151 We initiate the Kalman filter by assuming a prior estimate of $\mathbf{X}(t)$ at the first time epoch, de-
 152 noted $\mathbf{X}_{1|0}$, which has a sufficiently large covariance, denoted $\Sigma_{1|0}$, to effectively make our
 153 prior uninformed. For each time epoch t_i , Bayesian linear regression is used to incorporate
 154 GPS derived estimates of displacement with our prior estimate of the state $\mathbf{X}_{i|i-1}$ to form a
 155 posterior estimate of the state $\mathbf{X}_{i|i}$, which has covariance $\Sigma_{i|i}$. We then use the posterior es-
 156 timate of the state at time t_i to form a prior estimate of the state at time t_{i+1} through the transi-
 157 tion function

$$\mathbf{X}_{i+1|i} = \mathbf{F}_{i+1} \mathbf{X}_{i|i} + \delta_{i+1}, \quad (5)$$

158 where

$$\mathbf{F}_{i+1} = \begin{bmatrix} 1 & (t_{i+1} - t_i) & \mathbf{0} \\ 0 & 1 & \mathbf{0} \\ \mathbf{0} & \mathbf{0} & \mathbf{I} \end{bmatrix} \quad (6)$$

159 and δ_{i+1} is the process noise, which has zero mean and covariance described by

$$\mathbf{Q}_{i+1} = \sigma^2 \begin{bmatrix} \frac{(t_{i+1} - t_i)^3}{3} & \frac{(t_{i+1} - t_i)^2}{2} & \mathbf{0} \\ \frac{(t_{i+1} - t_i)^2}{2} & (t_{i+1} - t_i) & \mathbf{0} \\ \mathbf{0} & \mathbf{0} & \mathbf{0} \end{bmatrix}. \quad (7)$$

160 The covariance of the new prior state, $\mathbf{X}_{i+1|i}$, is then described by

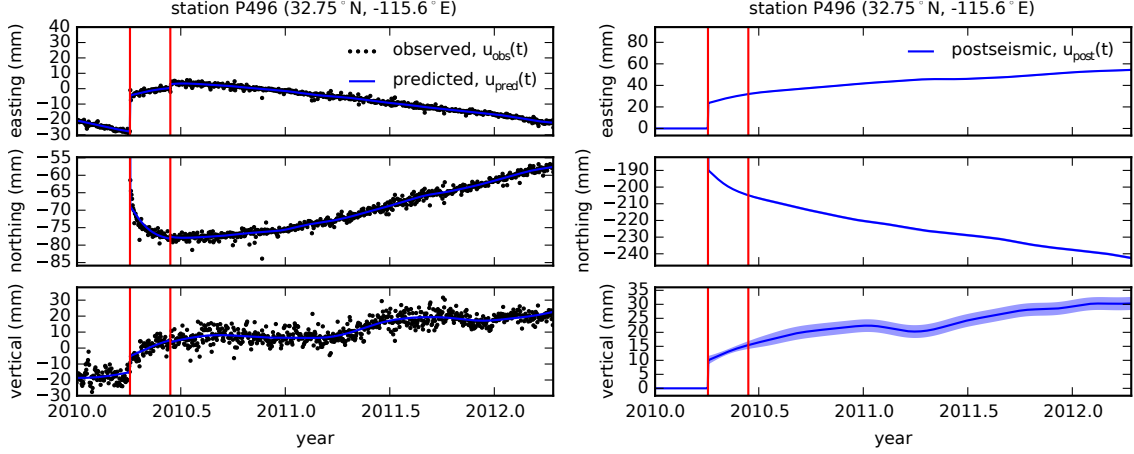
$$\Sigma_{i+1|i} = \mathbf{F}_{i+1} \Sigma_{i|i} \mathbf{F}_{i+1}^T + \mathbf{Q}_{i+1}. \quad (8)$$

161 This process is repeated for each of the N time epochs at which point we use Rauch-Tung-
 162 Striebel smoothing [Rauch *et al.*, 1965] to find $\mathbf{X}_{i|N}$, which is an estimate of the state at time
 163 t_i that incorporates GPS observation for all N time epochs. Our final estimates of $u_{\text{post}}(t)$
 164 are used in subsequent analysis, while the remaining components of the state vector are con-
 165 sidered nuisance parameters. In the interests of computational tractability, we down sample
 166 our smoothed time series from daily solutions down to weekly solutions.

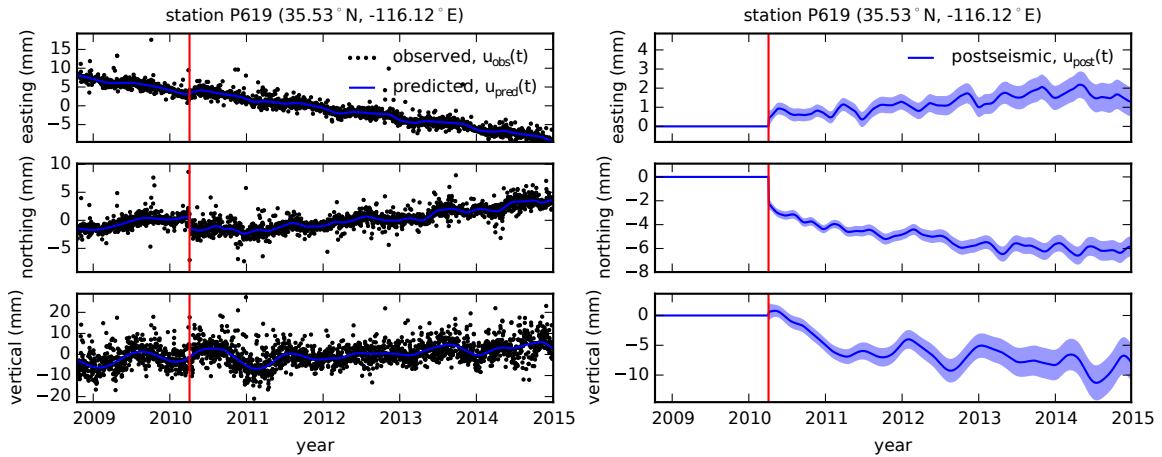
167 The smoothness of $u_{\text{post}}(t)$ is controlled by the chosen value of σ^2 , which describes how
 168 rapidly we expect postseismic displacements to vary over time. Setting σ^2 equal to zero will
 169 effectively result in modeling $u_{\text{post}}(t)$ as a straight line which is insufficient to describe the
 170 expected transient behavior in postseismic deformation. The other end member, where σ^2 is
 171 infinitely large, will result in $u_{\text{pred}}(t)$ over fitting the data. While one can use a maximum like-
 172 lihood based approach for picking σ^2 [e.g. Segall and Mathews, 1997], we instead take a sub-
 173 jective approach and choose a value for σ^2 that is just large enough to faithfully describe the
 174 observed deformation at the most near-field station in our study, P496, which exhibits the most
 175 pronounced rapid changes in velocity. This ensures that σ^2 will be sufficiently large so that
 176 our estimate of $u_{\text{post}}(t)$ does not smooth out potentially valuable postseismic signal at the re-
 177 maining stations. We find that using $\sigma^2 = 0.05 \text{m}^2/\text{yr}^3$ adequately describe all but the first
 178 week of postseismic deformation at station P496, which gets incorporated into our estimate
 179 of coseismic displacements (Figure 2). We assume that the first week of deformation is over-
 180 whelmingly the result of afterslip and this afterslip is lumped into our estimates of coseismic
 181 slip. Freed *et al.* [2007] noted that postseismic deformation can be observed at distances greater
 182 than 200 km from the Hector Mine earthquake and, after filtering the time series for stations
 183 up to 400 km from the El Mayor-Cucapah epicenter, we also clearly see far reaching postseis-
 184 mic transient deformation (Figure 3).

190 It is important to note that the shown uncertainties in $u_{\text{post}}(t)$ do not account for the non-
 191 negligible epistemic uncertainty in eq. (2). For example, we assume a constant rate of secu-
 192 lar deformation, which appears to be an appropriate approximation for all but perhaps the sta-
 193 tions closest to the Hector Mine epicenter, as noted above. Also, our model for seasonal de-
 194 formation in eq. (2) assumes a constant amplitude over time, which means that any yearly vari-
 195 ability in the climatic conditions could introduce systematic residuals [Davis *et al.*, 2012]. In-
 196 deed, it would be more appropriate to consider the seasonal amplitudes $c_2 - c_5$ in eq. (2) as
 197 stochastic variables [Murray and Segall, 2005]. By using constant seasonal amplitudes, our es-
 198 timate of $u_{\text{post}}(t)$ seems to describe some of the unmodeled annual and semi-annual oscilla-
 199 tions (e.g. Figure 3).

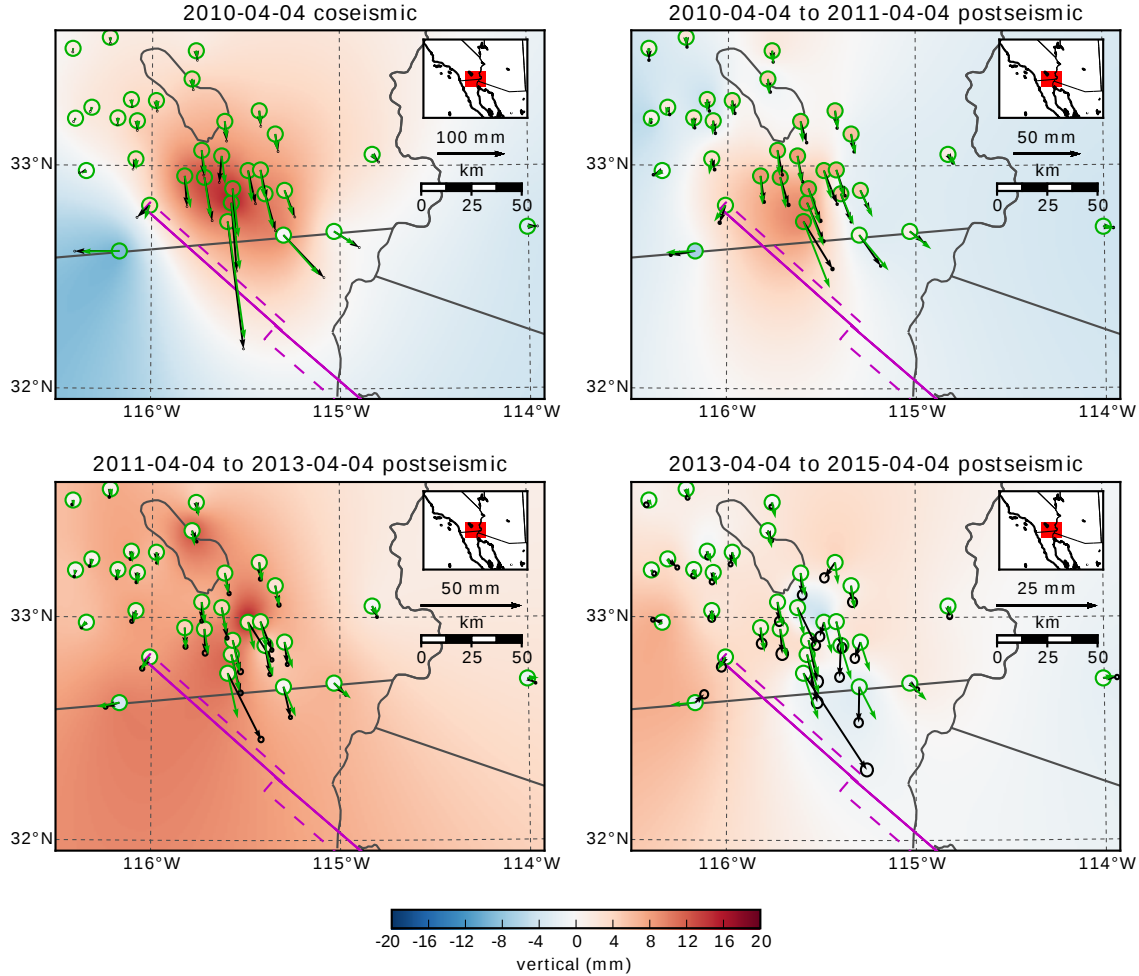
200 We show in Figures 4 and 5 the near and far-field postseismic displacements accumu-
 201 lated over the time intervals 0-1 years, 1-3 years, and 3-5 years, as well as the coseismic dis-
 202 placements. Stations at epicentral distances beyond ~ 200 km have an elevated rate of defor-
 203 mation for the first three years following the earthquake. This far-field deformation has a south-



185 **Figure 2.** Left panels show GPS time series from UNAVCO (black) and the predicted displacement (blue)
 186 from eq. (2) for a near-field station. Red lines indicate the times of the El Mayor-Cucapah and Ocotillo earth-
 187 quakes. The right panels show estimated coseismic and postseismic displacements u_{post} which are extracted
 188 from the predicted displacements. The 68% confidence interval is shown in light blue.



189 **Figure 3.** same as Figure 2 but for a far-field station.



214 **Figure 4.** Near-field coseismic and cumulative postseismic displacements over the indicated time periods
 215 (black) as well as predicted displacements for our preferred model from Section 3.3 (green). Observed verti-
 216 cal deformation is shown as an interpolated field and predicted vertical displacements are shown within the
 217 circles at the base of each vector. Note that the interpolant is not well constrained in Mexico where there is no
 218 data available.

204 ward trend along the direction of the El Mayor-Cucapah P axis and a similar eastward trend
 205 can be seen in the few far-field stations in Arizona, located along the T axis. After three years,
 206 the trend in far-field postseismic deformation is barely perceptible. Most far-field stations dis-
 207 play an initial subsidence for the first year after the El Mayor-Cucapah earthquake followed
 208 by continued uplift. This trend in vertical deformation can be observed in all three of the quad-
 209 rants where postseismic data is available, which means that the vertical deformation does not
 210 exhibit an anti-symmetric quadrant pattern, as would be expected for postseismic processes.
 211 Although we use vertical deformation in our analysis in Section 3, we do not put an empha-
 212 sis on trying to describe the vertical deformation as it likely does not have postseismic ori-
 213 gins.

220 The near-field postseismic deformation is notably sustained when compared to the far-
 221 field deformation. Namely, the station in this study which is closest to the El Mayor-Cucapah
 222 epicenter, P496, has been moving at a steady rate of ~ 1.5 cm/yr to the south since about one
 223 year after the El Mayor-Cucapah earthquake. Vertical postseismic deformation in the near-field
 224 does display a quadrant pattern which is consistent with the coseismic vertical deformation,

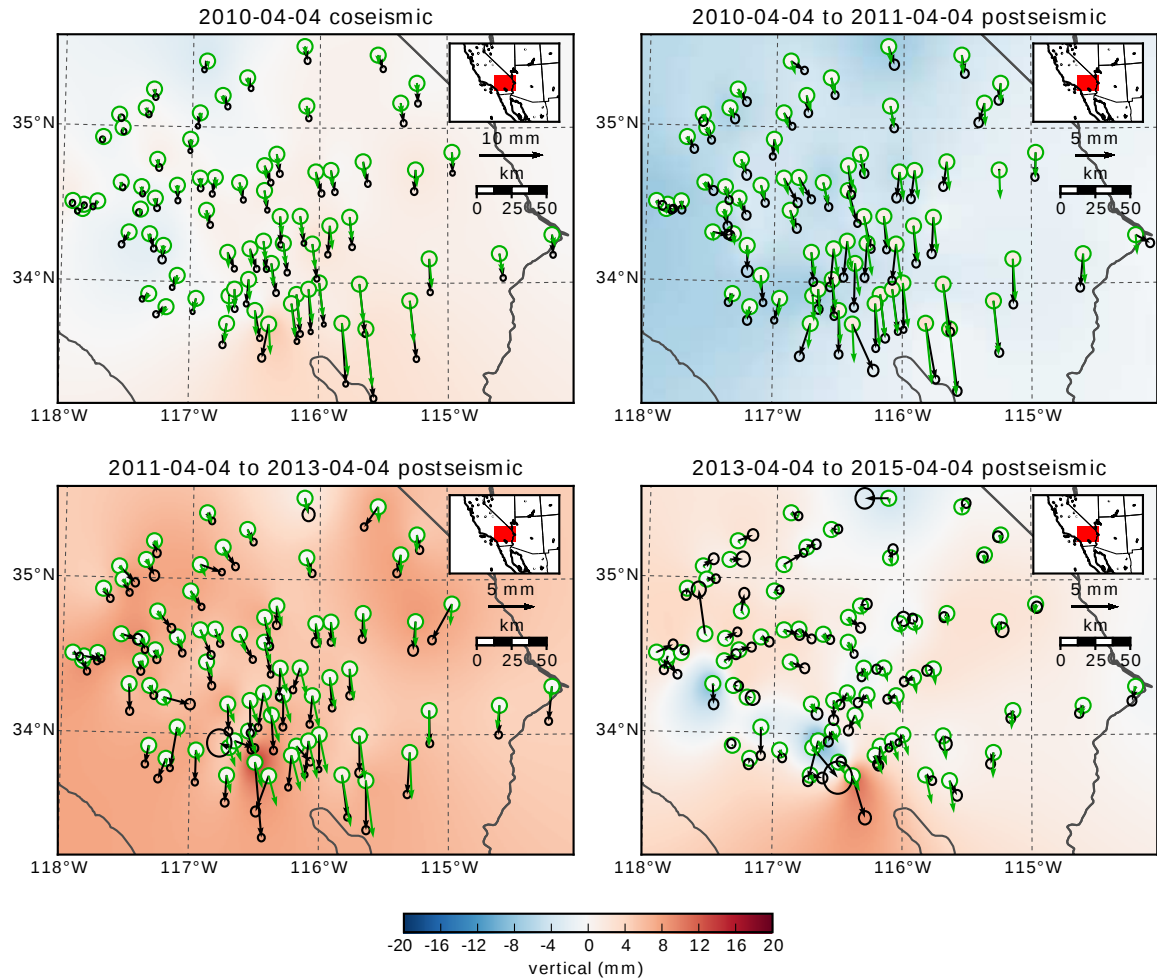


Figure 5. Same as Figure 4 but for far-field stations.

depth (km)	λ (GPa)	μ (GPa)	η_{eff} (10^{18} Pa s)	μ_k/μ
0-5	24.0	24.0	-	-
5-15	35.0	35.0	-	-
15-30	42.0	42.0	44.3	0.0
30-60	61.0	61.0	5.91	0.375
60-90	61.0	61.0	1.99	0.375
90-120	61.0	61.0	1.31	0.375
120-150	61.0	61.0	1.10	0.375
150- ∞	61.0	61.0	1.07	0.375

229 **Table 1.** Assumed and estimated material properties. λ and μ are assumed known *a priori* and are based
 230 on the values used for the coseismic model by *Wei et al.* [2011b]. The values for η_{eff} are estimated in Section
 231 3.2, and $\frac{\mu_k}{\mu}$ are the optimal shear moduli ratios found in Section 3.3 for a Zener rheology upper mantle.

225 suggesting that it is resulting from postseismic processes. However, the vertical postseismic
 226 signal is only apparent for the first year after the earthquake (Figure 4). As with the far-field
 227 deformation, there is a general trend of uplift in the near-field after about one year.

228 3 Postseismic Modeling

229 We seek to find the mechanisms driving five years of postseismic deformation following
 230 the El Mayor-Cucapah earthquake and we consider afterslip and viscoelastic relaxation as
 231 candidate mechanisms. Poroelastic rebound has also been used to model postseismic defor-
 232 mation [e.g. *Jónsson et al.*, 2003]; however, *Gonzalez-Ortega et al.* [2014] found that poroe-
 233 lastic rebound is unlikely to be a significant contributor to postseismic deformation following
 234 the El Mayor-Cucapah earthquake. Furthermore, we consider stations which are sufficiently
 235 far away from the main rupture that poroelastic rebound should be insignificant.

236 We estimate coseismic and time-dependent postseismic fault slip, both of which are as-
 237 sumed to occur on a fault geometry modified from *Wei et al.* [2011b]. Field studies [*Fletcher*
 238 *et al.*, 2014] and LIDAR observations [*Oskin et al.*, 2012] have revealed a significantly more
 239 complicated fault geometry than what was inferred by *Wei et al.* [2011b], especially within the
 240 Sierra Cucapah. However, we find that a relatively simple coseismic fault geometry based on
 241 [*Wei et al.*, 2011b] is adequate because most of the stations used in this study are sufficiently
 242 far from the El Mayor-Cucapah rupture zone that they are insensitive to the details in the fault
 243 geometry found by *Fletcher et al.* [2014] and *Oskin et al.* [2012]. The fault geometry used in
 244 this study (Figure 1) consists of the two main fault segments inferred by *Wei et al.* [2011b],
 245 where the northern segment runs through the Sierra Cucapah up to the US-Mexico border and
 246 the southern segment is the Indiviso fault which extends down to the Gulf of California. Both
 247 segments extend from the surface to 15 km depth. We extend the northern segment by 40 km
 248 to the north-west, motivated by the clustering of aftershocks on the northern tip of the coseis-
 249 mic rupture zone [*Hauksson et al.*, 2011; *Kroll et al.*, 2013]. This extended fault segment was
 250 also found to be necessary by *Rollins et al.* [2015] and *Pollitz et al.* [2012] in order to describe
 251 the postseismic deformation.

252 3.1 Elastic Postseismic Inversion

253 We consider a variety of rheologic models for the lower crust and upper mantle. The
 254 simplest rheologic model is to consider them to be effectively elastic and isotropic. In such
 255 case, the rheologic parameters consist of the Lamé parameters, λ and μ , which are reasonably
 256 well known and we use the same values used by *Wei et al.* [2011b] throughout this paper (Ta-
 257 ble 3). The only unknown is the distribution of fault slip, which can be easily estimated from
 258 postseismic deformation through linear least squares. Using a subset of the GPS stations con-

sidered in this study, *Rollins et al.* [2015] found that three years of postseismic deformation following the El Mayor-Cucapah earthquake can be explained with afterslip on the coseismic fault plane without requiring any viscoelastic relaxation. We also perform an elastic slip inversion, but we use GPS stations within a larger radius about the El Mayor-Cucapah epicenter (400 km instead of \sim 200 km). Our forward problem describing predicted postseismic deformation u_{pred} in terms of time dependent fault slip, s , is

$$u_{\text{pred}}(x, t) = \int_F s(\xi, t) g(x, \xi) d\xi, \quad (9)$$

where F denotes the fault and $g(x, \xi)$ is the elastic Green's function describing displacement at surface position x resulting from slip at ξ on the fault. We estimate coseismic slip and the rate of afterslip at the discrete time intervals, 0.0-0.125, 0.125-0.25, 0.5-1.0, 1.0-2.0, 2.0-3.0, 3.0-4.0, and 4.0-5.0 years after the earthquake. Each fault segment is discretized into roughly 4 km by 4 km patches and we estimate a strike-slip and thrust component of slip for each patch. We impose that the direction of slip and slip rate are within 45° of right-lateral. We also add zeroth-order Tikhonov regularization so that our solution for s satisfies

$$\min_s \left(\left\| \frac{u_{\text{pred}}(s) - u_{\text{post}}}{\sigma_{\text{post}}} \right\|_2^2 + \lambda_s \|s\|_2^2 \right), \quad (10)$$

where σ_{post} is the uncertainty on postseismic displacements and λ_s is a penalty parameter which is chosen with a trade-off curve. We use Pylith [Aagaard et al., 2013] to compute the Green's functions for this inversion as well as for the remaining inversions in this paper.

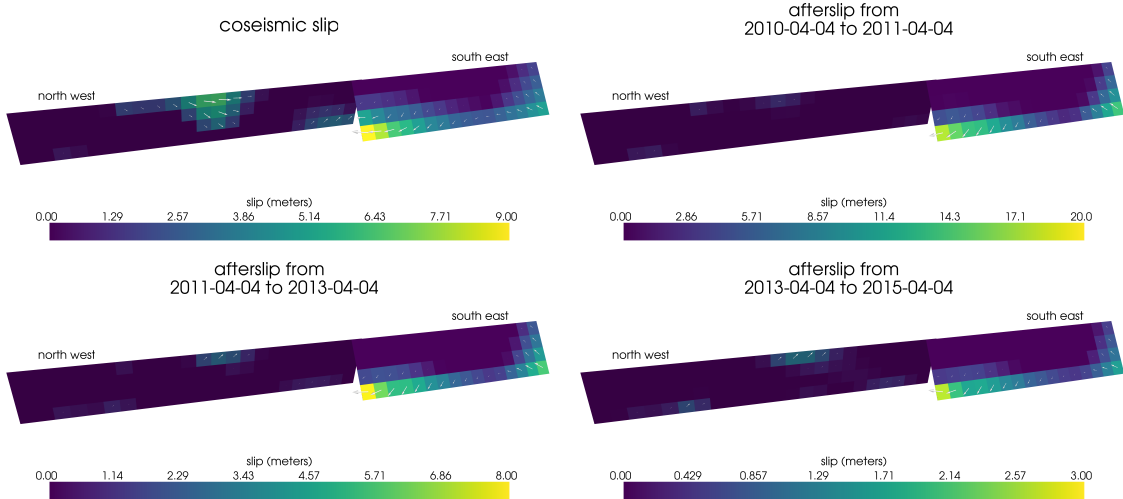
Our coseismic slip and afterslip solutions are shown in Figure 6. As with *Rollins et al.* [2015], we find that a large amount of afterslip on the southern fault segment is required to explain the observations. The potency of our inferred coseismic slip is $3.2 \times 10^9 \text{ m}^3$, equivalent to a Mw7.28 earthquake when assuming a shear modulus of 32 GPa. The potency of our inferred cumulative five years of afterslip is $6.1 \times 10^9 \text{ m}^3$, equivalent to a Mw7.46 earthquake, which is unrealistically large if we consider afterslip to be driven by coseismically induced stresses. Figure 7 shows the time series for the observed and predicted postseismic displacements at stations along the El Mayor-Cucapah P axis. We show the radial component of displacements with respect to the El Mayor-Cucapah epicenter and we also rescale the displacements so that the difference between the minimum and maximum observed displacements are the same for each station. Our elastic slip model accurately describes near-field postseismic deformation and systematically underestimates postseismic deformation at epicentral distances $\gtrsim 150 \text{ km}$. When the fault segments used in the inversion are extended down to 30 km depth, rather than 15 km, the systematic far-field residuals are smaller but remain apparent. Because an elastic model requires an unrealistic amount of afterslip and is unable to predict far-field deformation, we move on to consider viscoelastic models in the next section.

3.2 Early Postseismic Inversion

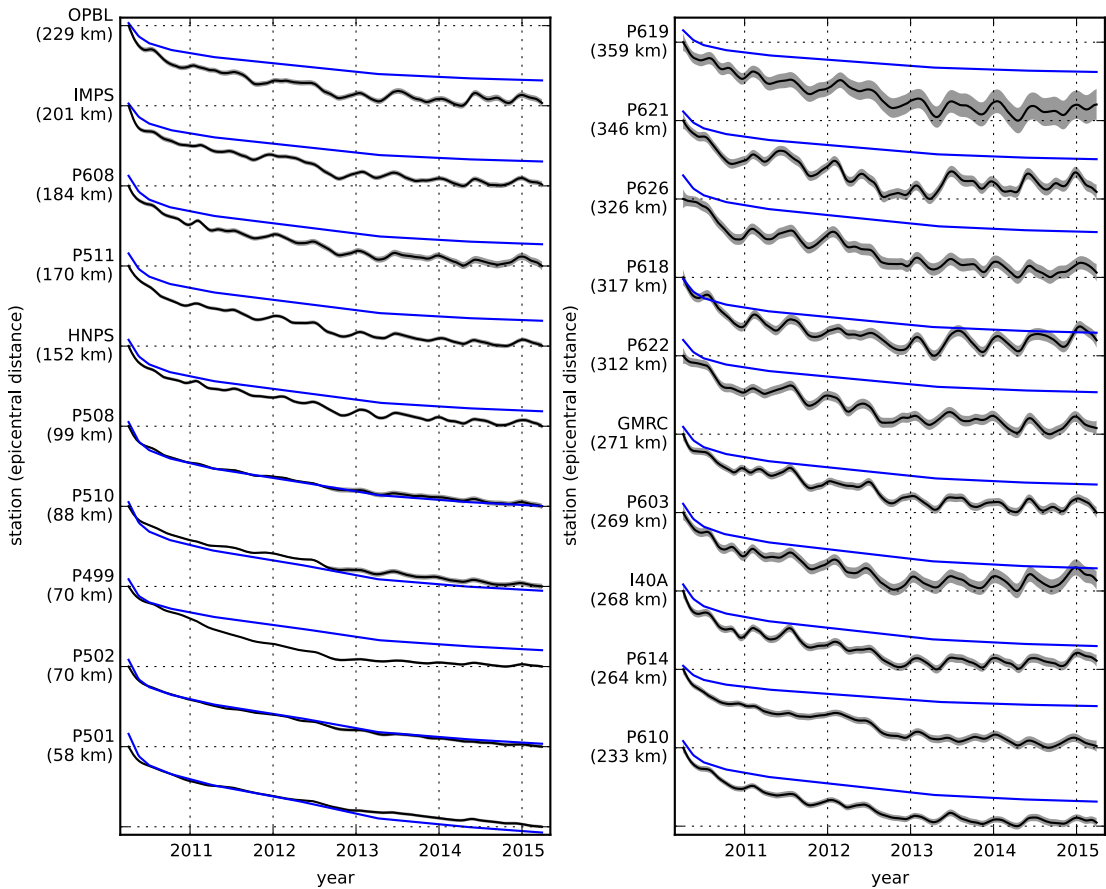
For any linear viscoelastic rheology of the crust and mantle, postseismic displacements resulting from time dependent fault slip can be described as

$$u_{\text{pred}}(x, t) = \int_F s(\xi, t) g(x, \xi) d\xi + \int_0^t \int_F s(\xi, \tau) f(t - \tau, x, \xi) d\xi d\tau, \quad (11)$$

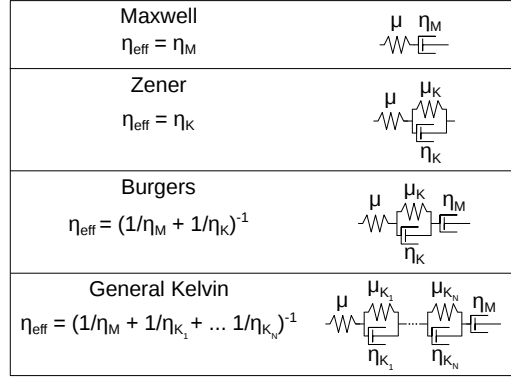
where $f(t, x, \xi)$ describes the time-dependent velocity at x resulting from viscoelastic relaxation of stresses induced by slip at ξ . f is a function of λ , μ , and any additional rheologic parameters controlling the viscoelastic response, which are generally not well known. Schematic representations of the viscoelastic rheologic models considered in this study are shown in Figure 8. We discuss these rheologic models and their use in geophysical studies in Section 4.



294 **Figure 6.** Coseismic slip and cumulative afterslip over the indicated intervals for the elastic model from
295 Section 3.1. Color indicates the magnitude of slip while arrows indicate the motion of the hanging wall.



296 **Figure 7.** Scaled radial component of observed postseismic displacements u_{obs} (black) and displacements
297 predicted by the best fitting elastic model u_{pred} (blue). Downward motion indicates that the station is moving
298 toward the El Mayor-Cucapah epicenter. Displacement time series are scaled so that the minimum and max-
299 imum observed values lie on the grid lines. The 68% confidence interval for the observed displacements are
300 shown in gray.



309 **Figure 8.** Schematic illustration of the rheologic models considered in this paper as well as their effective
310 viscosities.

311 In order to greatly simplify the inverse problem, we use the method described in *Hines and Hetland* [2016] to constrain an initial effective viscosity structure from the early postseismic
312 deformation. Our method utilizes the fact that coseismic stresses throughout the crust and
313 upper mantle depend on the instantaneous elastic parameters and are independent of the viscoelastic
314 parameters which we wish to estimate. Immediately following an earthquake, each
315 parcel will have a strain rate that is proportional to the coseismic stress and inversely proportional
316 to the parcel's effective viscosity, η_{eff} . Using one-dimensional viscoelastic models, we
317 define the effective viscosity as
318

$$\eta_{\text{eff}} = \left. \frac{\sigma}{\dot{\varepsilon}} \right|_{t=0}, \quad (12)$$

319 where σ is an applied stress at $t = 0$ and $\dot{\varepsilon}$ is the resulting strain rate. Figure 8 shows how
320 η_{eff} relates to the parameters for various linear viscoelastic rheologies. We can deduce that the
321 initial rate of surface deformation resulting from viscoelastic relaxation is a summation of the
322 surface deformation resulting from relaxation in each parcel, scaled by the reciprocal of the
323 parcel's effective viscosity. That is to say

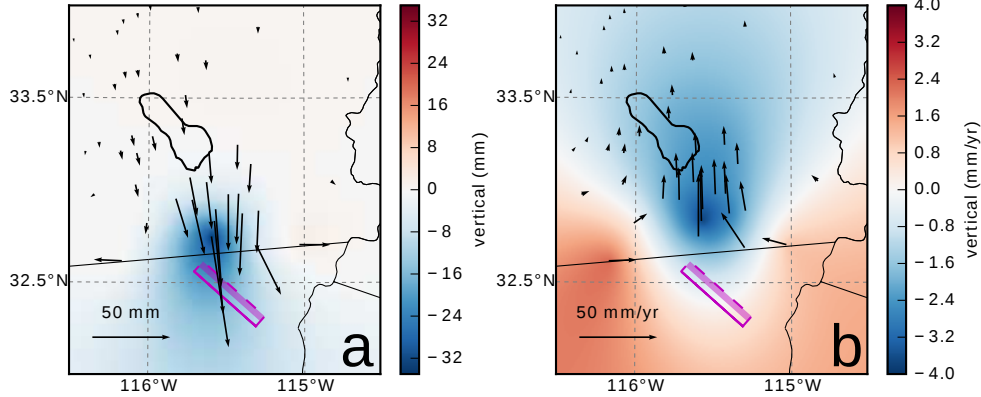
$$f(0, x, \xi) = \int_L \frac{h(x, \xi, \zeta)}{\eta_{\text{eff}}(\zeta)} d\zeta, \quad (13)$$

324 where L denotes the crust and mantle and $h(x, \xi, \zeta)$ describes the initial rate of deformation
325 resulting from viscoelastic relaxation at ζ induced by slip at ξ . We can combine eq. (13) with
326 eq. (11) to get a first order approximation for early postseismic deformation,

$$u_{\text{pred}}(x, t) \approx \int_F s(\xi, t) g(x, \xi) d\xi + \int_0^t \int_F \int_L \frac{s(\tau, \xi)}{\eta_{\text{eff}}(\zeta)} h(x, \xi, \zeta) d\zeta d\xi d\tau, \quad (14)$$

327 which is valid for as long as the rate of deformation resulting from viscoelastic relaxation is
328 approximately constant. Although eq. (14) may only be valid for a short portion of the post-
329 seismic period, its utility becomes apparent when noting that g and h are only functions of
330 the fault geometry and instantaneous elastic properties, λ and μ , and thus g and h can be com-
331 puted numerically as a preprocessing step. The forward problem in eq. (14) can then be rapidly
332 evaluated for any realization of s and η_{eff} . This is in contrast to evaluating the full forward
333 problem, eq. (11), numerically for each realization of s and the unknown rheologic proper-
334 ties.

335 Details on how eq. (14) is used to estimate s and η_{eff} from postseismic deformation can
336 be found in *Hines and Hetland* [2016]. A non-linear Kalman filter based inverse method can



365 **Figure 9.** Displacements resulting from fault slip at lower crustal depths (a), and initial velocities resulting
 366 from subsequent relaxation of a viscoelastic lower crust (b). The fault segment dips 75° to the north-east and
 367 its surface projection is outlined in magenta. The highlighted area on the fault extends from 15 to 30 km depth
 368 and indicates where 1 meter of right-lateral slip was imposed. The elastic properties of the crust and mantle
 369 are the same as in Table 3, and η_{eff} is 10^{18} Pa s in the lower crust. Vertical displacements are interpolated
 370 between station locations.

337 also be used to estimate s and η_{eff} in a manner akin to Segall and Mathews [1997] or McGuire
 338 and Segall [2003], in which we would not have to explicitly impose a time dependent parametriza-
 339 tion of s . We have thoroughly explored Kalman filter based approaches, but we ultimately pre-
 340 fer the method described in Hines and Hetland [2016] because of its relative simplicity. More-
 341 over, we believe the piecewise continuous representation of slip with respect to time to be suf-
 342 ficiently general for the resolving power of these GPS data.

343 We estimate coseismic slip and afterslip with the same spatial and temporal discretiza-
 344 tion as in Section 3.1. Simultaneously, we estimate η_{eff} within six vertically stratified layers
 345 which have depths ranging from 15–30 km, 30–60 km, 60–90 km, 90–120 km, 120–150 km,
 346 as well as from 150 km to the bottom of our numerical model domain at 800 km. We again
 347 restrict fault slip to occur between 0 and 15 km depth, which is done in order to help elim-
 348 inate inevitable non-uniqueness in the inversion. It has long been recognized that fault slip at
 349 sufficiently great depths can produce surface deformation that is indistinguishable from vis-
 350 coelastic relaxation, at least in two-dimensional earthquake models [Savage, 1990]. Addition-
 351 ally, we note that when simultaneously estimating both afterslip and viscosity in the lower crust,
 352 the inverse problem becomes particularly ill-posed. This ill-posedness is illustrated in Figure
 353 9, which shows the displacements resulting from a meter of slip on a fault extending from 15
 354 to 30 km depth and the initial velocity resulting from subsequent viscoelastic relaxation in the
 355 lower crust, which is given a viscosity of 10^{18} Pa s. In this demonstration, the viscoelastic re-
 356 laxation is entirely driven by the fault slip in the lower crust. The horizontal displacements
 357 from fault slip are in the opposite direction as the displacements resulting from viscoelastic
 358 relaxation. This means that surface displacements resulting from afterslip at lower crustal depths
 359 can be cancelled out, at least partially, by a low viscosity lower crust. We eliminate this null
 360 space by allowing only one mechanism in the lower crust, which we choose to be viscoelas-
 361 tic relaxation. This is not to say that we do not believe deep afterslip to be a possibility; rather,
 362 we restrict slip to seismogenic depths as a modeling necessity. Although, it has been noted
 363 that the pattern of vertical postseismic deformation following the El Mayor-Cucapah earthquake
 364 indicates that a significant amount of afterslip must be shallow [Rollins et al., 2015].

371 We must determine at which point the early postseismic approximation breaks down, which
 372 we will denote as t_{bd} . As noted, eq. (14) is valid for approximately as long as the rate of de-
 373 formation resulting from viscoelastic relaxation is approximately constant. We can almost cer-

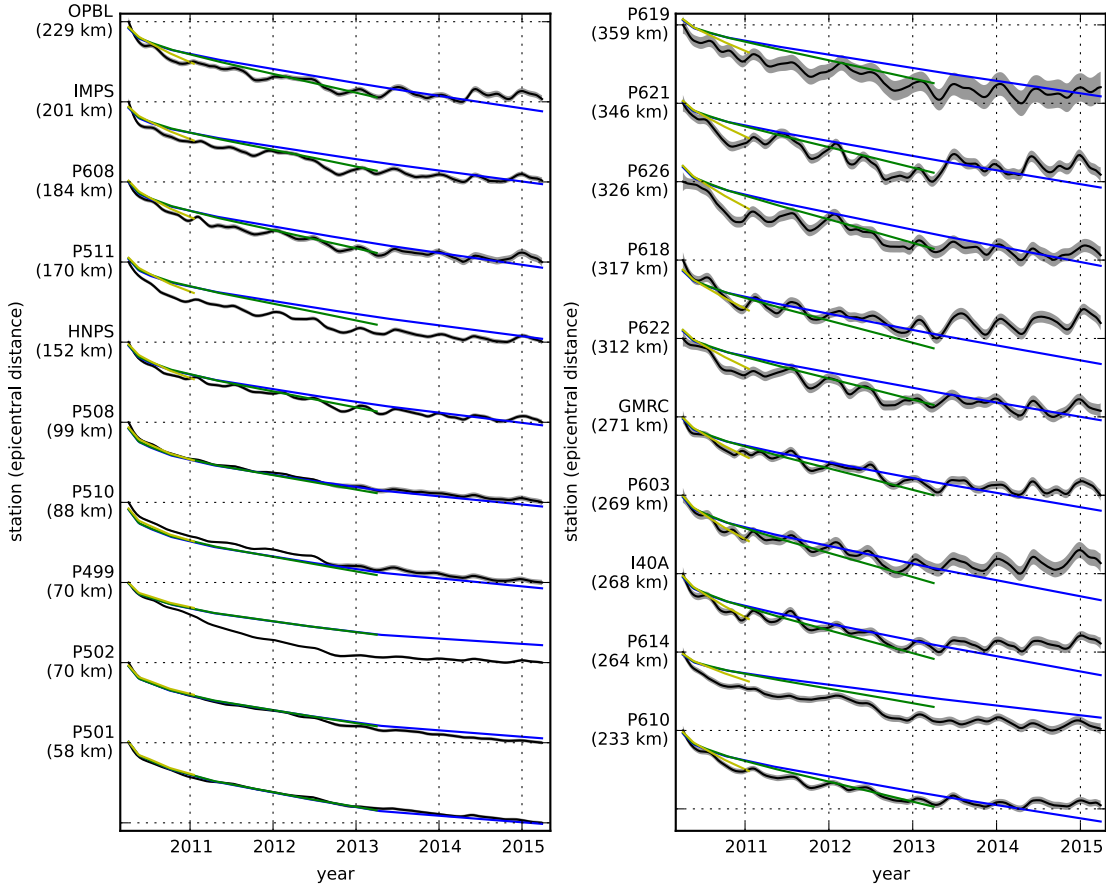


Figure 10. Observed postseismic displacements (black) and best fitting predictions of eq. (14) to 5.0 (blue), 3.0 (green), and 0.8 (yellow) years of the postseismic data.

tainly assume that deformation at the most far-field stations, which are ~ 400 km away from the El Mayor-Cucapah epicenter, is the result of viscoelastic relaxation. The approximation should then be valid for as long as a linear trend adequately approximates the far-field deformation. Using this logic, it would appear that t_{bd} is about one year after the El Mayor-Cucapah earthquake. Another way to determine t_{bd} is to find the best fitting prediction of eq. (14) to observed deformation using increasing durations of the postseismic time series. t_{bd} should be the point when eq. (14) is no longer capable of describing the observed deformation without incurring systematic misfits. When using eq. (14) to fit the entire five years of postseismic displacements, we see that the near-field displacements (e.g., station P501) are accurately predicted. When looking at displacements in the far-field (e.g., station P621), we see that eq. (14) overestimates the rate of deformation in the later postseismic period and underestimates the rate of deformation in the early period (Figure 10). Due to the low signal-to-noise ratios for far-field stations, it is difficult to determine at what point eq. (14) is no longer able to predict the observed displacements; however, we settle on $t_{bd} = 0.8$ years after the earthquake, while acknowledging that the choice is subjective. As noted in Hines and Hetland [2016], overestimating t_{bd} will result in a bias towards overestimating η_{eff} , while picking a t_{bd} which is too low will not necessarily result in a biased estimate of η_{eff} , although the uncertainties would be larger. We can then consider inferences of η_{eff} to be an upper bound on the viscosity needed to describe the far-field rate of deformation during the first 0.8 years of postseismic deformation.

We estimate coseismic slip, afterslip, and effective viscosities by solving

$$\min_{s, \eta_{\text{eff}}} \left(\left\| \frac{u_{\text{pred}}(s, \eta_{\text{eff}}) - u_{\text{post}}}{\sigma_{\text{post}}} \right\|_2^2 + \lambda_s \|s\|_2^2 + \lambda_\eta \|\nabla \eta_{\text{eff}}^{-1}\|_2^2 \right), \quad (15)$$

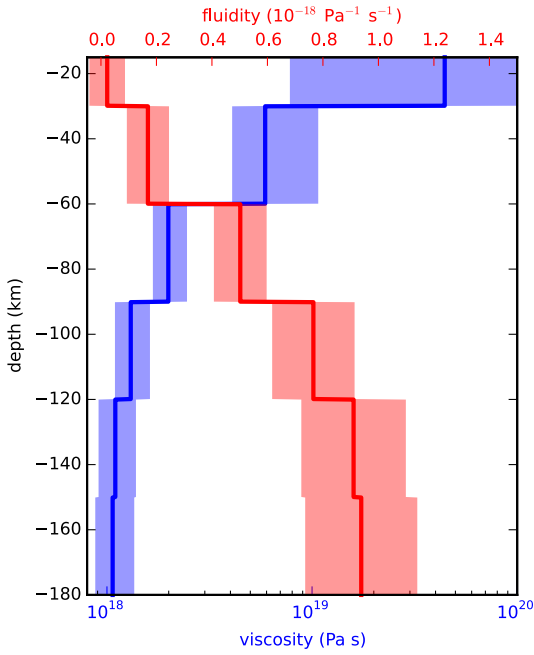
where u_{post} consists of the first 0.8 years of postseismic deformation and u_{pred} are the predicted displacements from eq. (14). Due to inherent non-uniqueness, we have added zeroth-order Tikhonov regularization to estimates of s and second-order Tikhonov regularization to estimates of effective fluidity η_{eff}^{-1} . The degree to which we impose the regularization on slip and fluidity is controlled by the penalty parameters λ_s and λ_η , which are chosen with trade-off curves. Our goal here is to get a prior constraint on η_{eff} to minimize the amount of searching we have to do when describing the postseismic deformation over the full five years, which we do in Section 3.3. Estimates of s made here will not be used in Section 3.3, and so the motivation behind adding regularization to s is to ensure that the slip driving viscoelastic relaxation in eq. (14) is sensible.

Our estimated effective viscosities, and corresponding fluidities, are shown in Figure 11. Although fluidity is rarely used in geophysical literature, eq. (13) is linear with respect to fluidity and so the fluidity indicates the amplitude of the viscoelastic signal coming from each layer. We also show the 95% confidence intervals for estimated viscosities and fluidities but we note that the uncertainties tend to be underestimated due to the added regularization [Aster *et al.*, 2011]. A robust feature that we see is that the largest jump in fluidity is at 60 km depth, which is consistent with the range of lithosphere-asthenosphere boundary depths inferred by Lekic *et al.* [2011]. This transitional depth is also consistent with the viscosity structure required to explain far-field postseismic deformation following the Hector Mine earthquake [Freed *et al.*, 2007]. We find that the viscosity below 60 km depth needs to be $\sim 10^{18}$ Pa s to describe the early rate of postseismic deformation at far-field stations while the lower crust and uppermost mantle need to be relatively stronger. The viscosity of the lower crust is the least well constrained as there is no evidence of relaxation in that layer, meaning that it is effectively elastic over the first 0.8 years after the earthquake.

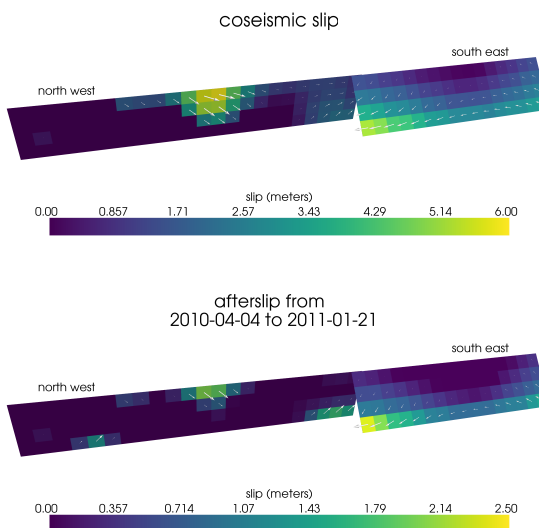
Our initial estimate for coseismic slip and cumulative afterslip over the first 0.8 years after the El Mayor-Cucapah earthquake are shown in Figure 12. Similar to our elastic slip model from Section 3.1, a significant amount of right-lateral and normal coseismic slip is inferred to be on the Sierra Cucapah fault segment. Our coseismic slip solution is consistent with field studies [Fletcher *et al.*, 2014] and the model from Wei *et al.* [2011b]. The potency of inferred coseismic slip is 3.3×10^9 m³, which is also about the same as that inferred from Section 3.1. The present inference of afterslip on the Indiviso fault is significantly less than what was found in the Section 3.1 where we did not account for viscoelasticity. When fault slip is simultaneously estimated with viscosity, the potency of inferred afterslip over the first 0.8 years after the earthquake is 0.85×10^9 m³, compared to 3.5×10^9 m³ when we assume the crust and upper mantle are elastic. The significant amount of afterslip inferred on the Indiviso fault seems to be compensating for unmodeled viscoelastic relaxation at depths greater than 60 km. The fact that there is still an appreciable amount of afterslip inferred on the Indiviso fault raises the question of whether it is compensating for viscoelastic relaxation that is more localized than what we allow for since we only estimate depth dependent variations in viscosity.

3.3 Full Postseismic Inversion

In the previous section, we used the inverse method from Hines and Hetland [2016] to constrain the effective viscosity structure required to explain the first 0.8 years of postseismic deformation. In this section, we use these effective viscosities as a prior constraint when searching for models which are capable of describing the available five years of postseismic data, where our forward problem is now eq. (11) rather than the approximation given by eq. (14). We perform a series of fault slip inversions assuming a variety of rheologies for the lower crust and upper mantle which are consistent with our findings from Section 3.2. We appraise each model using the mean chi-squared value,



421 **Figure 11.** Effective viscosities and associated fluidities inferred by fitting eq. (14) to the first 0.8 years of
 422 postseismic displacements. 95% confidence intervals, estimated from bootstrapping, are indicated by color
 423 fields.



439 **Figure 12.** Coseismic slip and afterslip inferred by fitting eq. (14) to the first 0.8 years of postseismic
 440 displacements.

$$\bar{\chi}^2 = \frac{1}{N} \left\| \frac{u_{\text{pred}} - u_{\text{obs}}}{\sigma_{\text{obs}}} \right\|_2^2, \quad (16)$$

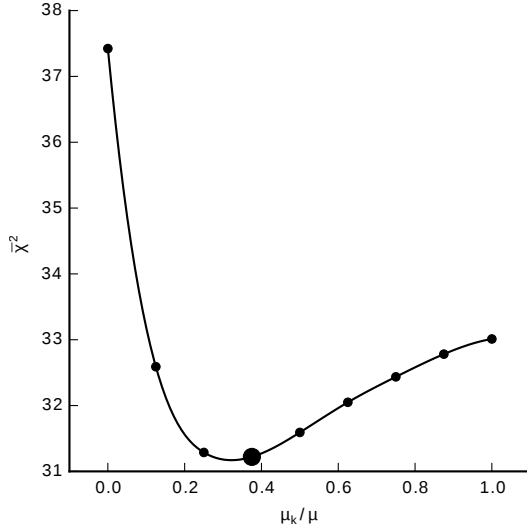
450 where N is the number of observations.

451 We first assume that the crust and mantle can be described with a Maxwell rheology,
 452 and we set the steady-state viscosity η_M equal to our inference of η_{eff} . We compute f and g
 453 from eq. (11) using Pylith, and we use the same spatial and temporal discretization of s as
 454 in Sections 3.1 and 3.2. We estimate s using linear least squares and find a misfit of $\bar{\chi}^2 =$
 455 37.4. For comparison, $\bar{\chi}^2 = 35.3$ for the elastic model from Section 3.1. The Maxwell vis-
 456 coelastic model has a larger misfit because it tends to overestimate the rate of deformation af-
 457 ter about three years (Figure 14). Since our initial estimates of η_{eff} may be biased towards over-
 458 estimating viscosities, we have also performed the slip inversion where we use uniformly lower
 459 viscosities in the crust and mantle. However, decreasing the viscosity only increases the mis-
 460 fit. Although, the viscosities used here are consistent with the successful Maxwell viscoelas-
 461 tic models found by *Rollins et al.* [2015] and *Spinler et al.* [2015], which had mantle viscosi-
 462 ties on the order of 10^{18} Pa s and relatively higher lower crustal viscosities, we find that such
 463 a model is incapable of describing the entire postseismic time series. *Pollitz et al.* [2001] sim-
 464 ilarly recognized this deficiency in a Maxwell rheology, which then motivated their exploration
 465 of a Burgers rheology upper mantle [*Pollitz*, 2003].

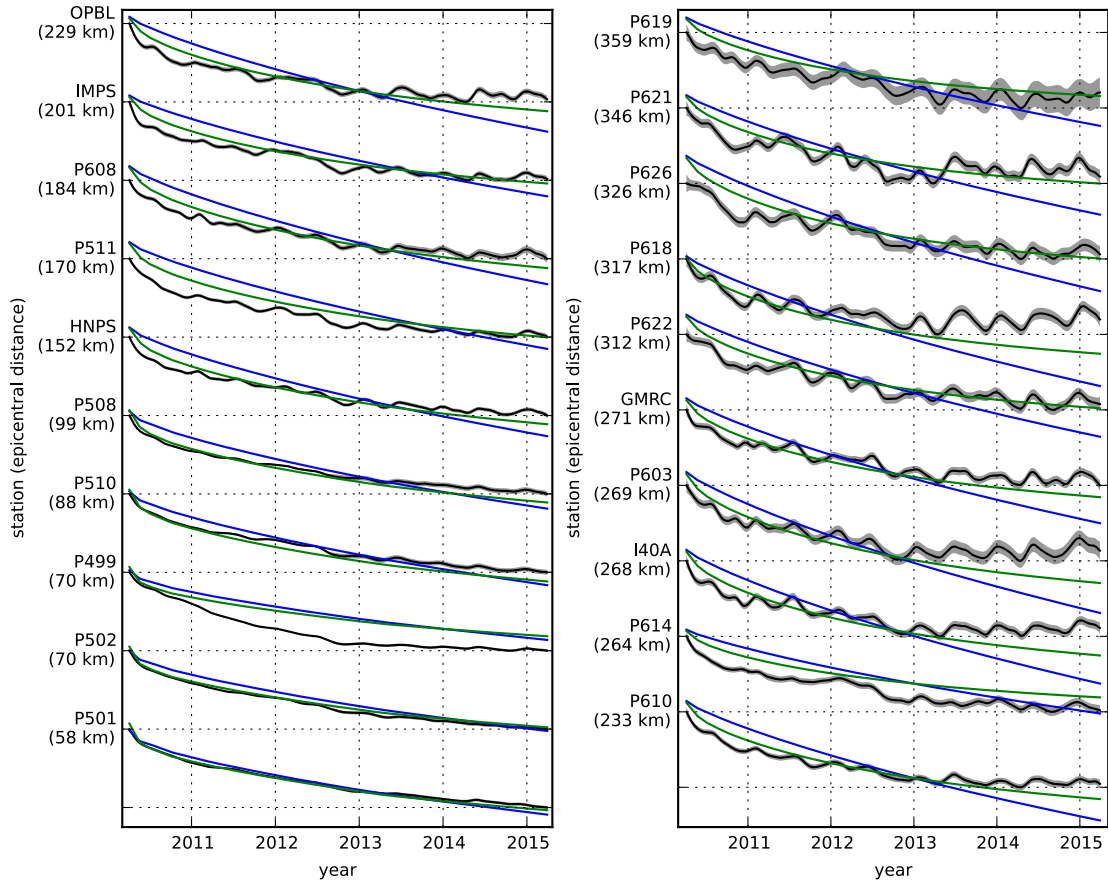
466 Instead of exploring a Burgers rheology mantle, which introduces two new parameters
 467 that need to be estimated, the transient viscosity η_K and transient shear modulus μ_K , we first
 468 consider a Zener rheology for the mantle, which only introduces one additional unknown pa-
 469 rameter, μ_K . We assume that the lower crust still has a Maxwell rheology. The steady-state
 470 viscosity in the crust and the transient viscosity in the mantle are set equal to the inferred ef-
 471 fective viscosities. We then estimate the ratio of shear moduli $\frac{\mu_K}{\mu}$. We compute nine differ-
 472 ent sets of Green's functions, f and g , where we assume values of $\frac{\mu_K}{\mu}$ ranging from 0 to 1.
 473 The former being a degenerate case where the Zener model reduces to the above Maxwell model.
 474 We estimate coseismic slip and afterslip for each realization of $\frac{\mu_K}{\mu}$. The shear moduli ratio
 475 that yields the best prediction to the observed postseismic displacements is found to be 0.375
 476 which produces a misfit of $\bar{\chi}^2 = 31.2$ (Figure 13). The improvement in the Zener model over
 477 the Maxwell model can be clearly seen in the fit to the far-field data (Figure 14). The Zener
 478 model does a significantly better job at explaining the transient rate of far-field deformation
 479 throughout the five years.

480 Because we are able to adequately describe the available five years of postseismic de-
 481 formation with a Zener model, we do not find it necessary to explore the parameter space for
 482 a more complicated Burgers rheology. However, since the Zener model is a Burgers model with
 483 an infinite steady-state viscosity, we can conclude that any Burgers rheology that has a tran-
 484 sient viscosity consistent with that found in Section 3.2 and a steady-state viscosity $\gtrsim 10^{20}$
 485 Pa s, which is effectively infinite on the time scale of five years, would also be able to sat-
 486 isfactorily describe the observable postseismic deformation.

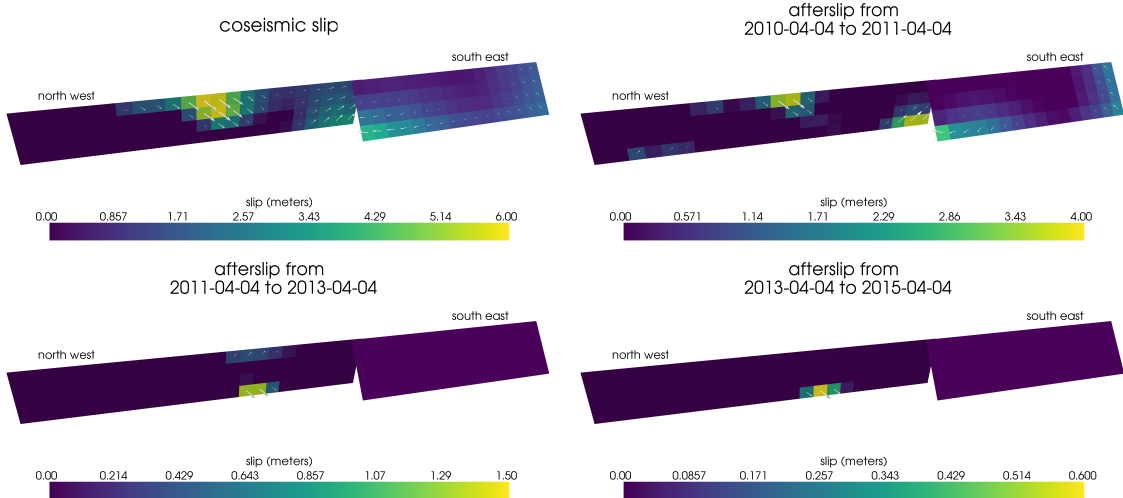
487 The regularized inference of coseismic slip and afterslip for our preferred Zener model
 488 is shown in Figure 15. The inferred coseismic potency is 3.0×10^9 m³, equivalent to a Mw7.26
 489 earthquake, and most of the slip is shallow and on the Sierra Cucapah fault segment. The po-
 490 tency of five years of afterslip is 1.1×10^9 m³. Most of the afterslip in our preferred model
 491 occurs within the first year after the earthquake and coincides with the location of our inferred
 492 coseismic slip. Inferred afterslip within the first year is accounting for the most rapid near-
 493 field transient deformation. After one year, afterslip is inferred to be deeper down on the Sierra
 494 Cucapah segment, which is describing much of the sustained near-field postseismic deforma-
 495 tion. We emphasize, that the GPS station closest to where we infer afterslip, P496, is still about
 496 30 km away, which is too far for us to conclusively argue for sustained localized deformation
 497 rather than shallow distributed deformation. The deep afterslip inferred after one year could
 498 potentially be describing deformation resulting from lower crustal flow. To test this, we have
 499 modified our preferred model by decreasing the lower crustal viscosity from 5.91×10^{19} Pa
 500



480 **Figure 13.** Mean chi-squared value for the best fitting slip model as a function of the transient shear modu-
 481 lus relative to the elastic shear modulus in a Zener upper mantle. Large dot indicates our preferred ratio.



482 **Figure 14.** Observed postseismic displacements (black). Predicted postseismic displacements for the best
 483 fitting slip model when assuming a Maxwell viscoelastic lower crust and upper mantle (blue). Predicted post-
 484 seismic displacements for the best fitting slip model when assuming a Maxwell viscoelastic lower crust and a
 485 Zener viscoelastic upper mantle (green). The effective viscosities are the same for both models and are shown
 486 in Figure 11.



529 **Figure 15.** Inferred coseismic slip and afterslip when assuming a Maxwell rheology in the lower crust and
 530 a Zener rheology in the upper mantle. The transient viscosity η_K in the mantle and steady-state viscosity η_M
 531 in the crust are set equal to the effective viscosities from Figure 11. We set $\frac{\mu_K}{\mu} = 0.375$ in the upper mantle.

507 s to 1×10^{19} Pa s, which is still consistent with our viscosity inference from Section 3.2, and
 508 inverted for fault slip. We find that a model with a weaker lower crust adequately describes
 509 the postseismic displacements without any afterslip after one year, while still requiring about
 510 the same amount of afterslip over the first year. We do believe that the early, shallow after-
 511 slip on the Sierra Cucapah segment is a robust feature in our preferred model, while we are
 512 not confident in our inference of later deep afterslip.

513 the postseismic displacements predicted by our preferred model are shown in Figures
 514 4, 5 and 14. Overall, the trends in the near-field and far-field transient deformation are accu-
 515 rately described. In particular, the trends in far-field deformation are much better described
 516 by our preferred Zener model than either an elastic model or a model with a Maxwell viscoelas-
 517 tic mantle (Figure 14). There are a few areas where we have notable misfit. Most of our mis-
 518 fit is for the near-field stations in the Imperial Valley, and we attribute this misfit to our rel-
 519 atively simple fault geometry, which does not account for potential fault slip in the Imperial
 520 Valley triggered by the El Mayor-Cucapah earthquake [Wei *et al.*, 2011a, 2015]. In particu-
 521 lar, we are unable to model the sustained, rapid rate of deformation at station P496, which sug-
 522 gests that this station could be influenced by a more localized deformation mechanism than
 523 is considered in this study. Additionally, we see systematic misfit in the later postseismic pe-
 524 riod west of the Landers and Hector Mine earthquakes, which may be the result of unmod-
 525 eled postseismic deformation resulting from those earthquakes. Lastly, there are clear discrep-
 526 ancies between the observed and predicted vertical deformation following the first year after
 527 the El Mayor Cucapah earthquake. We observe a broad uplift throughout Southern Califor-
 528 nia, which is inconsistent with any postseismic model.

532 4 Discussion

533 It has long been recognized that deep afterslip and viscoelastic relaxation following an
 534 upper crustal earthquake can result in similar horizontal ground deformation at the surface [e.g.
 535 Savage, 1990; Pollitz *et al.*, 2001; Hearn, 2003; Feigl and Thatcher, 2006]. The similarity of
 536 the horizontal postseismic deformation results in a non-uniqueness in inferences of afterslip
 537 or viscoelastic relaxation. In contrast, the spatial pattern of vertical postseismic deformation
 538 has been proposed to be a discriminant between deep afterslip and viscoelastic relaxation [e.g.

539 *Pollitz et al.*, 2001; *Hearn*, 2003]. It is, however, important to note that patterns of vertical de-
 540 formation are very sensitive to the depth-dependence of viscosity below the upper crust [Yang
 541 and Toksöz, 1981; *Hetland and Zhang*, 2014]. The similarity between deformation resulting
 542 from deep afterslip and viscoelastic relaxation of coseismic stresses is different from the ill-
 543 posedness described in Section 3.2. In our method, any inferred afterslip will also mechani-
 544 cally drive additional viscoelastic relaxation. The horizontal deformation resulting from deep
 545 afterslip will generally be in the opposite direction as horizontal deformation resulting from
 546 viscoelastic relaxation of subsequent stresses in the lower crust (Figure 9). As a result, there
 547 is a trade-off between inferences of deep afterslip and lower crustal viscosity. In our synthetic
 548 tests in *Hines and Hetland* [2016], we have found that inverting surface deformation for af-
 549 terslip and viscosity within the same depth interval tends to result in overestimated afterslip
 550 and an underestimated viscosity.

551 Most postseismic studies assume Maxwell viscoelasticity in the lower crust and upper
 552 mantle [e.g. *Nur and Mavko*, 1974; *Pollitz et al.*, 2000; *Hetland*, 2003; *Freed et al.*, 2006; *John-*
 553 *son et al.*, 2009; *Hearn et al.*, 2009], which is the simplest viscoelastic rheologic model. In South-
 554 ern California, postseismic studies following the Landers [*Pollitz et al.*, 2000], Hector Mine
 555 [*Pollitz et al.*, 2001], and El Mayor-Cucapah earthquake [*Spinler et al.*, 2015; *Rollins et al.*, 2015],
 556 have assumed Maxwell viscoelasticity in the lower crust and upper mantle and have inferred
 557 upper mantle viscosities on the order of 10^{17} to 10^{18} Pa s and lower crust viscosities $\gtrsim 10^{19}$
 558 Pa s. These postseismic studies are consistent with *Kaufmann and Amelung* [2000] and *Cava-*
 559 *alié et al.* [2007], who found that an upper mantle viscosity of 10^{18} Pa s and a crustal viscos-
 560 ity $\gtrsim 10^{20}$ Pa s are necessary to describe subsidence resulting from changes in loading from
 561 Lake Mead. This isostatic adjustment is a process with similar spatial and temporal scales as
 562 postseismic deformation, and thus the inferred viscosities of these two types of studies would
 563 likely agree. While these studies found viscosities that are consistent with our effective vis-
 564 cosities from Section 3.2, they are inconsistent with viscosity estimates made from geophys-
 565 ical processes that occur over longer time scales. For example, *Lundgren et al.* [2009] found
 566 that lower crust and upper mantle viscosities on the order of 10^{21} and 10^{19} Pa s, respectively,
 567 are needed to describe interseismic deformation along the Southern San Andreas fault zone
 568 in the Salton Sea region. An even higher mantle viscosity, on the order of 10^{20} Pa s, is re-
 569 quired to describe isostatic adjustment resulting from the draining of Lake Bonneville, which
 570 occurs on the time scales of 10^4 years [*Crittenden*, 1967; *Bills and May*, 1987].

571 An additional deficiency with the Maxwell rheology is that it predicts a steady decay
 572 in the rate of postseismic deformation over time, which fails to describe the commonly ob-
 573 served rapid, early transience followed by a relatively steady rate of postseismic deformation.
 574 One could explain the early transient postseismic deformation with fault creep and the later
 575 phase with relaxation in a Maxwell viscoelastic lower crust and upper mantle [e.g. *Hearn et al.*,
 576 2009; *Johnson et al.*, 2009]. However, postseismic deformation at distances greater than ~ 200
 577 km from the El Mayor-Cucapah epicenter can only be attributed to viscoelastic relaxation [*Freed*
 578 *et al.*, 2007] and we have demonstrated that the far-field deformation cannot be explained with
 579 a Maxwell rheology (Figure 14).

580 We found that a Zener rheology in the upper mantle with a transient viscosity of $\sim 10^{18}$
 581 Pa s does a noticeably better job at predicting far-field postseismic deformation. A general-
 582 ization of the Zener viscoelastic model, schematically represented as several Kelvin elements
 583 connected in series, is commonly used to describe seismic attenuation [*Liu et al.*, 1976]. The
 584 highest viscosity needed to describe seismic attenuation is on the order of 10^{16} Pa s [*Yuen and*
 585 *Peltier*, 1982] which has a characteristic relaxation time on the order of days. Even though
 586 our inferred transient viscosity is orders of magnitude larger than that required for seismic at-
 587 tenuation models, the two models are not incompatible. Rather, the delayed elasticity in seis-
 588 mic attenuation models occurs on such short time scales that it can be considered part of the
 589 instantaneous elastic phase of deformation associated with the preferred Zener model in this
 590 study.

591 Of course, it has long been recognized that a Zener rheology provides an incomplete de-
 592 scriptions of the asthenosphere, as it does not have the fluid-like behavior required to explain
 593 isostatic rebound or convection in the mantle [O'Connell, 1971]. Yuen and Peltier [1982] pro-
 594 posed a Burgers rheology with a low transient viscosity ($\eta_K \approx 10^{16}$ Pa s) and high steady-
 595 state viscosity ($\eta_M \approx 10^{21}$ Pa s) to describe both seismic attenuation and long term geologic
 596 processes. The justification of a Burger's rheology mantle is further supported by laboratory
 597 experiments on olivine [Chopra, 1997]. Pollitz [2003] sought to describe postseismic defor-
 598 mation following Hector Mine with a Burgers rheology mantle and they found a best fitting
 599 transient viscosity of 1.6×10^{17} Pa s and steady-state viscosity of 4.6×10^{18} Pa s. While
 600 the Burgers rheology was introduced as a means of bridging the gap between relaxation ob-
 601 served in long and short term geophysical processes, the inferred steady state viscosity from
 602 Pollitz [2003] is still inconsistent with the Maxwell viscosities inferred from studies on the earth-
 603 quake cycle and Lake Bonneville. The transient viscosity inferred by Pollitz [2003] is constrained
 604 by the earliest phase of postseismic deformation following the Hector Mine earthquake. While
 605 Pollitz [2003] ruled out deep afterslip as an alternative mechanism based on inconsistent ver-
 606 tical deformation, it is still possible to successfully describe all components of early postseis-
 607 mic deformation following the Hector Mine earthquake with afterslip at seismogenic depths
 608 [Jacobs et al., 2002]. It is then possible that the preferred rheologic model from Pollitz [2003]
 609 was biased towards inferring a particularly low transient viscosity by neglecting to account for
 610 afterslip. This is in contrast to the present study, where we have inferred a viscosity structure
 611 simultaneously with afterslip. We also argue that a transient rheology is necessary to explain
 612 postseismic deformation; however, our preferred transient viscosity of $\sim 10^{18}$ Pa s in the up-
 613 per mantle is an order of magnitude larger than the transient viscosity found by Pollitz [2003].
 614 Since a Zener model is able to describe the available postseismic deformation following the
 615 El Mayor-Cucapah earthquake, any Burgers rheology with a steady-state viscosity that is \gtrsim
 616 10^{20} Pa s, effectively infinite over five years, would also be able to describe the postseismic
 617 deformation. Such a Burgers model might then be consistent with the steady-state viscosities
 618 necessary for lake loading, interseismic deformation, and mantle dynamics.

619 5 Conclusion

620 We have extracted a filtered and smoothed estimate of postseismic deformation follow-
 621 ing the El Mayor-Cucapah earthquake from GPS displacement time series. Our estimated post-
 622 seismic deformation reveals far-field (epicentral distances beyond ~ 200 km) transient defor-
 623 mation which is largely undetectable after about three years. Near-field deformation exhibits
 624 transience that decays to a sustained, elevated rate after about one or two years. We found that
 625 near-field transient deformation can be explained with shallow afterslip, and the sustained rate
 626 of near-field deformation can either be explained with continued afterslip or viscoelastic re-
 627 laxation in the lower crust. Far-field transient deformation can be more definitively ascribed
 628 to viscoelastic relaxation at depths greater than ~ 60 km. Beneath that depth, a transient vis-
 629 cosity of $\sim 10^{18}$ Pa s is required to describe the rate of far-field deformation throughout the
 630 five years considered in this study. By describing the available postseismic deformation with
 631 a transient rheology in the mantle, our preferred model does not conflict with the generally
 632 higher steady-state viscosities inferred from geophysical processes occurring over longer time
 633 scales.

634 Acknowledgements

635 We thank Andy Freed for an illuminating discussion on the data used in this study. This
 636 material is based on EarthScope Plate Boundary Observatory data services provided by UN-
 637 AVCO through the GAGE Facility with support from the National Science Foundation (NSF)
 638 and National Aeronautics and Space Administration (NASA) under NSF Cooperative Agree-
 639 ment No. EAR-1261833. The data used in this study can be found at www.unavco.org. This
 640 material is based upon work supported by the National Science Foundation under Grant Num-
 641 bers EAR 1045372 and EAR 1245263.

642 **References**

- 643 Aagaard, B. T., M. G. Knepley, and C. A. Williams (2013), A domain decomposition
 644 approach to implementing fault slip in finite-element models of quasi-static and dy-
 645 namic crustal deformation, *Journal of Geophysical Research: Solid Earth*, 118, doi:
 646 10.1002/jgrb.50217.
- 647 Argus, D. F., M. B. Heflin, G. Peltzer, F. Crampé, and F. H. Webb (2005), Interseismic
 648 strain accumulation and anthropogenic motion in metropolitan Los Angeles, *Journal of*
 649 *Geophysical Research: Solid Earth*, 110(4), 1–26, doi:10.1029/2003JB002934.
- 650 Aster, R. C., B. Borchers, and C. H. Thurber (2011), Parameter Estimation and Inverse
 651 Problems, vol. 90, Academic Press.
- 652 Bawden, G. W., W. Thatcher, R. S. Stein, K. W. Hudnut, and G. Peltzer (2001), Tectonic
 653 contraction across Los Angeles after removal of groundwater pumping effects., *Nature*,
 654 412(August), 812–815, doi:10.1038/35090558.
- 655 Bills, B. G., and G. M. May (1987), Lake Bonneville: Constraints on Lithospheric Thick-
 656 ness and Upper Mantle Viscosity From Isostatic Warping of Bonneville, Provo, and
 657 Gilbert Stage Shorelines, *Journal of Geophysical Research-Solid Earth and Planets*,
 658 92(B11), 11,493–11,508, doi:10.1029/JB092iB11p11493.
- 659 Çakir, Z., S. Ergintav, H. Özener, U. Dogan, A. M. Akoglu, M. Meghraoui, and
 660 R. Reilinger (2012), Onset of aseismic creep on major strike-slip faults, *Geology*,
 661 40(12), 1115–1118, doi:10.1130/G33522.1.
- 662 Cavalié, O., M. P. Doin, C. Lasserre, and P. Briole (2007), Ground motion measurement in
 663 the Lake Mead area, Nevada, by differential synthetic aperture radar interferometry time
 664 series analysis: Probing the lithosphere rheological structure, *Journal of Geophysical*
 665 *Research: Solid Earth*, 112(3), 1–18, doi:10.1029/2006JB004344.
- 666 Cetin, E., Z. Çakir, M. Meghraoui, S. Ergintav, and A. M. Akoglu (2014), Extent and
 667 distribution of aseismic slip on the İsmetpasa segment of the North Anatolian Fault
 668 (Turkey) from Persistent Scatterer InSAR, *Geochemistry, Geophysics, Geosystems*, 15,
 669 doi:10.1002/2014GC005307.Received.
- 670 Chopra, P. N. (1997), High-temperature transient creep in olivine rocks, *Tectonophysics*,
 671 279, 93–111, doi:10.1016/S0040-1951(97)00134-0.
- 672 Crittenden, M. (1967), Viscosity and Finite Strength of the Mantle as Determined from
 673 Water and Ice Loads*, *Geophysical Journal of the Royal Astronomical ...*, pp. 261–279,
 674 doi:10.1111/j.1365-246X.1967.tb06243.x.
- 675 Davis, J. L., B. P. Wernicke, and M. E. Tamisiea (2012), On seasonal signals in geode-
 676 tic time series, *Journal of Geophysical Research: Solid Earth*, 117(1), 1–10, doi:
 677 10.1029/2011JB008690.
- 678 Feigl, K. L., and W. Thatcher (2006), Geodetic observations of post-seismic transients in
 679 the context of the earthquake deformation cycle, *Comptes Rendus - Geoscience*, 338,
 680 1012–1028, doi:10.1016/j.crte.2006.06.006.
- 681 Fletcher, J. M., O. J. Teran, T. K. Rockwell, M. E. Oskin, K. W. Hudnut, K. J. Mueller,
 682 R. M. Spelz, S. O. Akciz, E. Masana, G. Faneros, E. J. Fielding, S. Leprince, A. E.
 683 Morelan, J. Stock, D. K. Lynch, A. J. Elliott, P. Gold, J. Liu-Zeng, A. González-
 684 Ortega, A. Hinojosa-Corona, and J. González-García (2014), Assembly of a large
 685 earthquake from a complex fault system: Surface rupture kinematics of the 4 April
 686 2010 El Mayor-Cucapah (Mexico) Mw 7.2 earthquake, *Geosphere*, 10(4), 797–827,
 687 doi:10.1130/GES00933.1.
- 688 Freed, A. M., R. Bürgmann, E. Calais, J. Freymueller, and S. Hreinsdóttir (2006), Impli-
 689 cations of deformation following the 2002 Denali, Alaska, earthquake for postseismic
 690 relaxation processes and lithospheric rheology, *Journal of Geophysical Research: Solid*
 691 *Earth*, 111, 1–23, doi:10.1029/2005JB003894.
- 692 Freed, A. M., R. Bürgmann, and T. Herring (2007), Far-reaching transient motions after
 693 Mojave earthquakes require broad mantle flow beneath a strong crust, *Geophysical*
 694 *Research Letters*, 34, 1–5, doi:10.1029/2007GL030959.

- 695 Gonzalez-Ortega, A., Y. Fialko, D. Sandwell, F. A. Nava-pichardo, J. Fletcher,
 696 J. Gonzalez-garcia, B. Lipovsky, M. Floyd, and G. Funning (2014), El Mayor-
 697 Cucapah (Mw7.2) earthquake: early near-field postseismic deformation from In-
 698 Sar and GPS observations, *Journal of Geophysical Research*, **119**, 1482–1497, doi:
 699 10.1002/2013JB010193.Received.
- 700 Hauksson, E., J. Stock, K. Hutton, W. Yang, J. A. Vidal-Villegas, and H. Kanamori
 701 (2011), The 2010 Mw 7.2 El mayor-cucapah earthquake sequence, Baja Califor-
 702 nia, Mexico and Southernmost California, USA: Active seismotectonics along the
 703 Mexican pacific margin, *Pure and Applied Geophysics*, **168**(3918), 1255–1277, doi:
 704 10.1007/s00024-010-0209-7.
- 705 Hearn, E. H. (2003), What can GPS data tell us about the dynamics of post-seismic defor-
 706 mation ?, (2003), 753–777.
- 707 Hearn, E. H., S. McClusky, S. Ergintav, and R. E. Reilinger (2009), Izmit earthquake post-
 708 seismic deformation and dynamics of the North Anatolian Fault Zone, *Journal of Geo-
 709 physical Research: Solid Earth*, **114**(August 2008), 1–21, doi:10.1029/2008JB006026.
- 710 Hetland, E. A. (2003), Postseismic relaxation across the Central Nevada Seismic Belt,
 711 *Journal of Geophysical Research*, **108**(Figure 2), 1–13, doi:10.1029/2002JB002257.
- 712 Hetland, E. A., and G. Zhang (2014), Effect of shear zones on post-seismic deformation
 713 with application to the 1997 Mw 7.6 manyi earthquake, *Geophysical Journal Interna-
 714 tional*, **198**, 259–269, doi:10.1093/gji/ggu127.
- 715 Hines, T. T., and E. A. Hetland (2013), Bias in estimates of lithosphere viscosity from
 716 interseismic deformation, *Geophysical Research Letters*, **40**(16), 4260–4265, doi:
 717 10.1002/grl.50839.
- 718 Hines, T. T., and E. A. Hetland (2016), Rapid and simultaneous estimation of fault slip
 719 and heterogeneous lithospheric viscosity from post-seismic deformation, *Geophysical
 720 Journal International*, **204**(1), 569–582, doi:10.1093/gji/ggv477.
- 721 Jacobs, A., D. Sandwell, Y. Fialko, and L. Sichoix (2002), The 1999 (Mw7.1) Hector
 722 Mine, California, Earthquake: Near-Field Postseismic Deformation from ERS Interfer-
 723 ometry, *Bulletin of the Seismological Society of America*, **92**(May), 1433–1442.
- 724 Johnson, K. M., and P. Segall (2004), Viscoelastic earthquake cycle models with deep
 725 stress-driven creep along the San Andreas fault system, *Journal of Geophysical Research
 726 B: Solid Earth*, **109**, 1–19, doi:10.1029/2004JB003096.
- 727 Johnson, K. M., R. Bürgmann, and J. T. Freymueller (2009), Coupled afterslip and vis-
 728 coelastic flow following the 2002 Denali Fault, Alaska earthquake, *Geophysical Journal
 729 International*, **176**(3), 670–682, doi:10.1111/j.1365-246X.2008.04029.x.
- 730 Jónsson, S., P. Segall, R. Pedersen, and G. Bjornsson (2003), Post-earthquake ground
 731 movements correlated to pore-pressure transients, *Nature*, **424**(July), 179–183, doi:
 732 10.1038/nature01758.1.
- 733 Kaufmann, G., and F. Amelung (2000), Reservoir-induced deformation and continental
 734 rheology in vicinity of Lake Mead, Nevada, *Journal of Geophysical Research*, **105**(B7),
 735 16,341, doi:10.1029/2000JB900079.
- 736 Kroll, K. A., E. S. Cochran, K. B. Richards-Dinger, and D. F. Sumy (2013), Aftershocks
 737 of the 2010 Mw 7.2 El Mayor-Cucapah earthquake reveal complex faulting in the Yuha
 738 Desert, California, *Journal of Geophysical Research: Solid Earth*, **118**(October), 6146–
 739 6164, doi:10.1002/2013JB010529.
- 740 Lekic, V., S. W. French, and K. M. Fischer (2011), Lithospheric Thinning Beneath Rifted
 741 Regions of Southern California, *Science*, **334**(November), 783–787.
- 742 Liu, H.-P., D. L. Anderson, and H. Kanamori (1976), Velocity dispersion due to anelastic-
 743 ity; implications for seismology and mantle composition, *Geophysical Journal Interna-
 744 tional*, **47**(1), 41–58, doi:10.1111/j.1365-246X.1976.tb01261.x.
- 745 Lundgren, P., E. A. Hetland, Z. Liu, and E. J. Fielding (2009), Southern San Andreas-San
 746 Jacinto fault system slip rates estimated from earthquake cycle models constrained by
 747 GPS and interferometric synthetic aperture radar observations, *Journal of Geophysical
 748 Research: Solid Earth*, **114**(2), 1–18, doi:10.1029/2008JB005996.

- 749 McGuire, J. J., and P. Segall (2003), Imaging of aseismic fault slip transients recorded
 750 by dense geodetic networks, *Geophysical Journal International*, 155(3), 778–788, doi:
 751 10.1111/j.1365-246X.2003.02022.x.
- 752 Meade, B. J., and B. H. Hager (2005), Block models of crustal motion in southern Cal-
 753 ifornia constrained by GPS measurements, *Journal of Geophysical Research B: Solid*
 754 *Earth*, 110, 1–19, doi:10.1029/2004JB003209.
- 755 Murray, J. R., and P. Segall (2005), Spatiotemporal evolution of a transient slip event on
 756 the San Andreas fault near Parkfield, California, *Journal of Geophysical Research : Solid*
 757 *Earth*, 110(9), 1–12, doi:10.1029/2005JB003651.
- 758 Nur, A., and G. Mavko (1974), Postseismic viscoelastic rebound, *Science*, 183(4121),
 759 204–206, doi:10.1038/098448b0.
- 760 O'Connell, R. J. (1971), Rheology of the Mantle, *EOS, Transactions, American Geophys-*
 761 *ical Union*, 52, 140–142.
- 762 Osokin, M. E., J. R. Arrowsmith, A. Hinojosa Corona, A. J. Elliott, J. M. Fletcher, E. J.
 763 Fielding, P. O. Gold, J. J. Gonzalez Garcia, K. W. Hudnut, J. Liu-Zeng, and O. J. Teran
 764 (2012), Near-field deformation from the El Mayor-Cucapah earthquake revealed by
 765 differential LIDAR, *Science*, 335(6069), 702–705, doi:10.1126/science.1213778.
- 766 Pollitz, F., C. Wicks, and W. Thatcher (2001), Mantle Flow Beneath a Continental Strike-
 767 Slip Fault : Postseismic Deformation After the 1999 Hector Mine Earthquake, *Science*,
 768 1814(2001), 1814–1818, doi:10.1126/science.1061361.
- 769 Pollitz, F. F. (2003), Transient rheology of the uppermost mantle beneath the Mo-
 770 jave Desert, California, *Earth and Planetary Science Letters*, 215, 89–104, doi:
 771 10.1016/S0012-821X(03)00432-1.
- 772 Pollitz, F. F., G. Peltzer, and R. Bürgmann (2000), Mobility of continental mantle: Evi-
 773 dence from postseismic geodetic observations following the 1992 Landers earthquake,
 774 *Journal of Geophysical Research*, 105(1999), 8035, doi:10.1029/1999JB900380.
- 775 Pollitz, F. F., R. Bürgmann, and W. Thatcher (2012), Illumination of rheological mantle
 776 heterogeneity by the M7.2 2010 El Mayor-Cucapah earthquake, *Geochemistry, Geo-*
 777 *physics, Geosystems*, 13(6), 1–17, doi:10.1029/2012GC004139.
- 778 Rauch, H. E., F. Tung, and C. T. Striebel (1965), Maximum likelihood estimates of linear
 779 dynamic systems, *AIAA Journal*, 3(8), 1445–1450.
- 780 Riva, R. E. M., and R. Govers (2009), Relating viscosities from postseismic relaxation to
 781 a realistic viscosity structure for the lithosphere, *Geophysical Journal International*, 176,
 782 614–624, doi:10.1111/j.1365-246X.2008.04004.x.
- 783 Rollins, C., S. Barbot, and J.-P. Avouac (2015), Postseismic Deformation Following the
 784 2010 M7.2 El Mayor-Cucapah Earthquake : Observations , Kinematic Inversions , and
 785 Dynamic Models, *Pure and Applied Geophysics*, doi:10.1007/s00024-014-1005-6.
- 786 Savage, J. C. (1990), Equivalent strike-slip earthquake cycles in half-space and
 787 lithosphere-asthenosphere earth models, *Journal of Geophysical Research*, 95, 4873,
 788 doi:10.1029/JB095iB04p04873.
- 789 Savage, J. C., and J. L. Svart (2009), Postseismic relaxation following the 1992 M 7.3
 790 Landers and 1999 M 7.1 Hector Mine earthquakes , southern California, *Journal of*
 791 *Geophysical Research*, 114(B01401), doi:10.1029/2008JB005938.
- 792 Savage, J. C., J. L. Svart, and S. B. Yu (2005), Postseismic relaxation and transient creep,
 793 *Journal of Geophysical Research: Solid Earth*, 110, 1–14, doi:10.1029/2005JB003687.
- 794 Segall, P., and M. Mathews (1997), Time dependent inversion of geodetic data, *Journal of*
 795 *Geophysical Research*, 102.
- 796 Spinler, J. C., R. A. Bennett, C. Walls, L. Shawn, and J. J. G. Garcia (2015), As-
 797 sessing long-term postseismic deformation following the M7.2 4 April 2010, El
 798 Mayor-Cucapah earthquake with implications for lithospheric rheology in the
 799 Salton Trough, *Journal of Geophysical Research: Solid Earth*, 120, 3664–3679, doi:
 800 10.1002/2014JB011613.Received.
- 801 Wei, M., D. Sandwell, Y. Fialko, and R. Bilham (2011a), Slip on faults in the Imperial
 802 Valley triggered by the 4 April 2010 Mw 7.2 El Mayor-Cucapah earthquake revealed by

- 803 InSAR, *Geophysical Research Letters*, 38(January), 1–6, doi:10.1029/2010GL045235.
- 804 Wei, M., Y. Liu, Y. Kaneko, J. J. McGuire, and R. Bilham (2015), Dynamic triggering of
805 creep events in the Salton Trough, Southern California by regional M5.4 earthquakes
806 constrained by geodetic observations and numerical simulations, *Earth and Planetary
807 Science Letters*, 427, 1–10, doi:10.1016/j.epsl.2015.06.044.
- 808 Wei, S., E. Fielding, S. Leprince, A. Sladen, J.-P. Avouac, D. Helmberger, E. Hauksson,
809 R. Chu, M. Simons, K. Hudnut, T. Herring, and R. Briggs (2011b), Superficial sim-
810 plicity of the 2010 El MayorCucapah earthquake of Baja California in Mexico, *Nature
811 Geoscience*, 4(9), 615–618, doi:10.1038/ngeo1213.
- 812 Yang M., and M. N. Toksöz (1981), Time-dependent deformation and stress relaxation
813 after strike-slip earthquakes, *Journal of Geophysical Research*, 86, 2889–2901.
- 814 Yuen, D. A., and W. R. Peltier (1982), Normal modes of the viscoelastic earth, *Geo-
815 physical Journal of the Royal Astronomical Society*, 69, 495–526, doi:10.1111/j.1365-
816 246X.1982.tb04962.x.